buildings

MDPI

Article

Physical Test and Numerical Analysis of Damage Mechanism of Rocky Foundation with Parallel Structural Surfaces

Ziguang Zhang *, Wanyu Li, Ankang Hu and Liang Wu

Anhui Province Key Laboratory of Building Structure and Underground Engineering, Anhui Jianzhu University, Hefei 230601, China; lwy1129@stu.ahjzu.edu.cn (W.L.); huankang5795@stu.ahjzu.edu.cn (A.H.); wl001@stu.webvpn.ahjzu.edu.cn (L.W.)

* Correspondence: phdzzg@ahjzu.edu.cn

Abstract: The growth of rock structural surfaces makes the deformation and stability analysis of rock pits more complex and challenging than that of soil pits. To investigate the damage mechanism of this foundation and provide ideas for foundation support, the paper constructed a simplified model by approximate plane analysis and dimensionless analysis of the similarity principle. The physical model was constructed from a mixture of materials, and then foundation excavation and loading tests were completed. The strain value of the strain gauges increased in stages in the range of 0–250. Excavation of the structural surface resulted in an increased number of deformation mutations. This type of rocky foundation damage underwent three stages: overburden crack development, cumulative deformation of the S-S, and collapse of the sliding body. Furthermore, numerical simulations corresponding to the physical model tests were set and used to validate and complement the physical tests. When the line loads reached 70.83 kN/m and 127.5 kN/m, the plastic zone of the structural surface was completely penetrated and the sliding body collapsed. The results of the studies can serve as a useful reference and guide for the excavation and support design of real-world rock foundation projects that are similar.

Keywords: rocky foundation pit; damage mechanism; parallel development of structural surfaces; physical model test and numerical simulation

Academic Editor: Humberto Varum

Received: 14 December 2024
Revised: 13 January 2025
Accepted: 14 January 2025
Published: 24 January 2025

Citation: Zhang, Z.; Li, W.; Hu, A.; Wu, L. Physical Test and Numerical Analysis of Damage Mechanism of Rocky Foundation with Parallel Structural Surfaces. *Buildings* **2025**, *15*, 371. https://doi.org/10.3390/buildings15030371

1. Introduction

Pit support engineering has always been a popular topic in the field of civil engineering. Scholars and engineers are dedicated to investigating or developing idealistic pit support structures due to the range of challenging environmental conditions in pits and the increasingly desirable engineering economic performance requirements [1–3]. The main issue with the foundation pit excavation project is the steady deformation and damage progression of the supporting structure. However, the primary issue for the rocky pit's ability to stabilize itself should be the deformation damage mechanism of the pit excavation. Wei Yan et al. [4] used the myopic plane damage method for soil–rocky foundation excavation stability calculations. Yan reckoned the maximum permissible vertical excavation depth of the pit, H_{max}, was calculated theoretically, and it was noted that H_{max} was not only related to its (cohesion) c, (angle of internal friction) φ, (volumetric weight) γ, and (upper load) q, but also inversely proportional to the soil–rock ratio. However, rock formations of rocky foundation pits often have developed structural surfaces and rich yield in practice, which leads to complex calculations of the deformation and stability of rocky foundation pits. Some scholars had gone from uniaxial and shear tests of pore-size-dilated rock mass and nonpersistent and persistent jointed rock to study their mechanical behavior and to

characterize them accurately in terms of rock mechanics [5–7]. Other scholars had considered the more realistic development of rock masses in reality, mainly from sophisticated modeling tools. Mariam Al-E'Bayat et al. [8] used a Lattice Spring-Based Synthetic Rock Mass Model to analyze the effect of the inclination of the structural face on the stability factor of safety and the structural face spacing on the damage region influence mechanism. Huajin Zhang et al. [9] innovated a robust method for rock slope stability assessment that employed Latin hypercubes to realistically fit the characteristic parameters of the actual geotechnical structural surfaces; Dongjie Hua et al. [10] conducted an in-depth study on the elastic wave velocity of nodular rock bulk. At the same time, scholars have undertaken a lot of research on the damage mechanism of complex rock bodies with different conditions. Jintao Wang and Jianpin Zuo [11] revealed the damage mechanism of rock mass under tension; Linfeng Zhu et al. [12] elucidated the mechanism by which anchors controlled the shear creep behavior of rock joints; Jin Xu et al. [13,14] derived an analytical equation for the upper limit stability coefficient of a large inclined rocky upright pit slope containing a cavern. However, there is not much in-depth research on the damage mechanism of rocky foundation pits in strata with parallel development of structural surfaces.

For the study of pit slope engineering, in addition to numerical computational analysis [15–17], the physical model test with numerical computational analysis is also a highly reliable and widely used method [18–21]. Xiongyu Hu et al. [22] analyzed the behavior of a new type of support system in anisotropic joints by conducting physical modeling tests on tunnel tube sheet lining; Nader Moussaei et al. [23] classified the damage mechanisms of laminated rock tunnels into nine categories using both physical modeling and numerical simulation. Jutao Qiu et al. [24] investigated the mechanical behavior and damage characteristics of subway tunnels under mixed strata at burial depths of 50–500 m through physical model tests; Jiong Wang et al. [25] revealed the mechanical properties of NPR cords in soft rock through large-scale physical modeling tests and obtained the mechanical properties of steel-reinforced rock bodies; Gang Wei et al. [26] used a self-developed loading device to accomplish the internal force response law of the Hangzhou subway shield structure section under pit unloading.

The mentioned findings provided ideas for studying the damage mechanism of rocky foundation pits with parallel structural surfaces. Figure 1 shows the schematic for the methodology followed in this paper. We first determined similar ratios, similar materials, and similar ratios for the physical model tests. Specific similarity ratios were derived based on dimensionless analysis. Secondly, the casting of the physical model mainly was completed through installed formwork, mixed material, compacted material, taken-off formwork, cured structure, and attached strain gauges. Then excavation and loading tests on the physical model were performed, respectively. The results explored the strain change characteristics and damage process of the foundation. Finally, numerical modeling was performed as a two-dimensional model. The setup of the numerical simulation was kept consistent with the setup of the physical model tests. The numerical simulation calculations validated and complemented the physical tests.

2. Physical Model Test

In the team's previous study [27], we used the deep foundation pit of the Ningxia Road subway in Qingdao as a prototype and simplified this rocky foundation pit into a planar model. Then the self-stabilizing control effect modeling tests were conducted for FPVRW. In addition, the modeling tests made the assumption that the 3D effect of the foundation pit corners was not taken into account, and the orthogonal tests were used to determine similar materials and similar ratios. The above assumptions and experimental practices apply equally to the physical modeling tests in this thesis. Distinguishing from

the previous study, this thesis considers the role of the influence of the upper soil layers of rocky foundation. This is due to the uneven thickness of the upper soil layer of a rocky foundation in an actual deep foundation project.

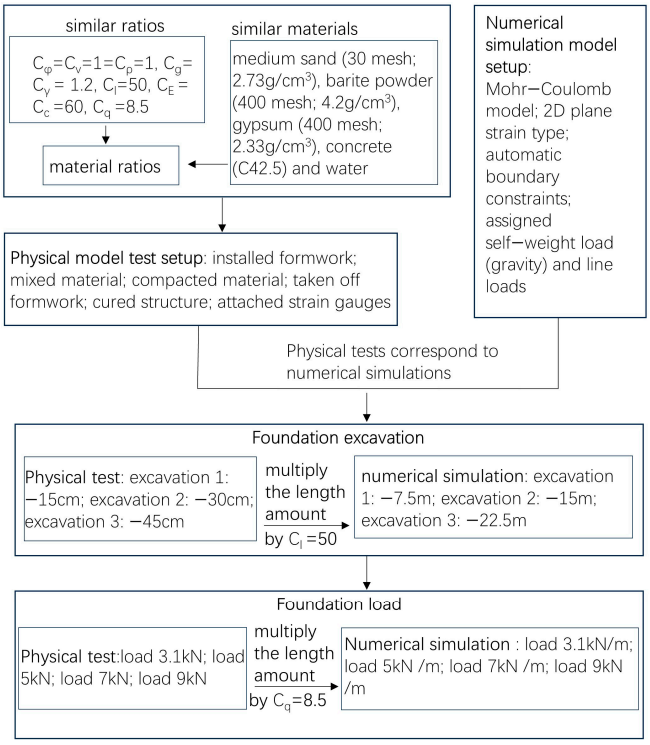

Figure 1. The schematic for methodology.

2.1. Similar Ratios and Similar Material

The similarity principle is used to represent the proportionality that should be satisfied between physical quantities within a prototype or model and is the basis for determining similarity conditions. The three commonly used methods for deriving the similarity principle are law analysis, equation analysis, and dimensionless analysis. Based on the similarity principle, dimensionless analysis was used to derive similar indicators. The specific projection process was as follows:

The parameters involved in this physical modeling test are geometric dimension (l), density (ρ), acceleration (g), volumetric weight (γ), cohesion (c), angle of internal friction (φ), Young's modulus (E), Poisson's ratio (v), and line load (q). The similarity ratio of the parameters (l, ρ, g, γ, c, φ, E, v, and q) is the ratio of the model to the prototype's parameters, respectively denoted as C_l, C_ρ, C_g, C_γ, C_c, C_φ, C_E, C_v, and C_q.

According to the second law of the similarity principle, the functional equation of these physical quantities is expressed in the general functional Equation (1).

$$f(l,\ \rho,\ g,\ \gamma,\ \varphi,\ E,\ v,\ c,\ q) = 0 \tag{1}$$

Assume that l, ρ, and g are fundamental physical quantities. According to the π-theorem Equation (1) can be written as

$$f(\pi_1, \pi_2, \pi_3, \pi_4, \pi_5, \pi_6) = 0 \tag{2}$$

Convert the function Equation (2) into a power series. Take π_6 as an example:

$$\pi_6 = \frac{q}{l^a \rho^b g^c} = \frac{\left[MT^{-2}\right]}{[L]^a \left[ML^{-3}\right]^b \left[LT^{-2}\right]^c} = M^{1-b} L^{-a+3b-c} T^{-2+2c} \quad (3)$$

Since π_6 is a dimensionless quantity, it follows that

$$\begin{cases} 1-b=0 \\ -a+3b-c=0 \\ -2+2c=0 \end{cases} \Rightarrow \begin{cases} a=2 \\ b=1 \\ c=1 \end{cases}$$

Substituting the calculations of a, b, and c into Equation (3) yields Equation (4).

$$\pi_6 = \frac{q}{l^2 \rho^1 g^1} \quad (4)$$

The similarity indicator, $C_q = \sqrt{C_l} C_\rho C_g$, can be obtained from Equation (4). Similarly, it is known that $C_c = C_E = C_l C_\rho C_g$, $C_\gamma = C_\rho C_g$, and $C_\varphi = C_v$. Since the cohesion c and Poisson's ratio v are dimensionless quantities, it is assumed that $C_\varphi = C_v = 1$. As needed for the physical modeling tests, it is assumed that $C_l = 50$, $C_\rho = 1$, and $C_g = 1.2$; thus, $C_\gamma = 1.2$, $C_c = C_E = 60$, and $C_q = 8.5$.

The mechanical parameters of the prototype pit rock formation were shown in Table 1 for raw material. Uniaxial compression and straight shear tests were performed on similar materials in the previous study of our team [27], and so the specific physico–mechanical parameters of the similar material were obtained, as shown in Table 1. The ratio of the mechanical parameters of the raw material and similar material was its corresponding similarity ratio.

Table 1. The mechanical parameters of the raw material and similar material.

Parameter Type		v	φ/(°)	γ/(kN/m³)	E/(MPa)	c/(kPa)
Similarity ratio		$C_v = 1$	$C_\varphi = 1$	$C_\gamma = 1.2$	$C_E = 60$	$C_c = 60$
Rock structure (R-S)	raw material	0.25	35	22.5	5000	600
	similar material	0.25	35	18.75	83.33	10
Structural surface (S-S)	raw material	0.38	30	20.5	50	100
	similar material	0.38	30	17.08	0.83	1.67

Table 2 gives the material ratios of the rock structure (R-S) and structural surface (S-S) in the physical model. The material used in this test is a mixture material commonly employed in geotechnical physical modeling tests, which comprises medium sand, barite powder, gypsum, concrete, and water, as seen in Table 3. The physical modeling tests in this thesis used the same materials, material ratios, and similar ratios as in the team's previous study.

Table 2. The material ratio of the rock structure (R-S) and structural surface (S-S).

Classification	Ratio of Concrete and Gypsum	Ratio of Water and Solid Material	Ratio of Cementitious Material and B-P&S	Ratio of Barite Powder and Sand
Rock structure (R-S)	1:1	1:7	1:30	1:10
Structural surface (S-S)	1:1	1:7	1:30	0:10

Note: the B-P&S is barite powder and sand.

Table 3. Specifications of similar materials.

Similar Material Types	Medium Sand	Barite Powder	Gypsum	Concrete
fineness specification density	30 mesh 2.73 g/cm^3	400 mesh 4.2 g/cm^3	400 mesh 2.33 g/cm^3	C42.5

2.2. Physical Model Test Setup

The dimensions of the test model box are 1.5 m in length, 1 m in width, and 1.2 m in height. And the box consists of four iron plates and a piece of tempered glass. The type of strain gauges used in the test was BX120-30AA geotechnical foil resistance strain gauges (produced in Xingdongfang Group Company, Chengdu, China). These strain gauges were pasted on the 10 points (A_0, A, B, C, D, G, H, L, M, N, while A_0 is the compensation point) as depicted in Figure 2. The loading test of the foundation pit was conducted using an electro–hydraulic servo pressurization system. The loading system can apply a load of 500 kN, with a test force resolution of 0.01 kN and a displacement resolution of 0.01 mm.

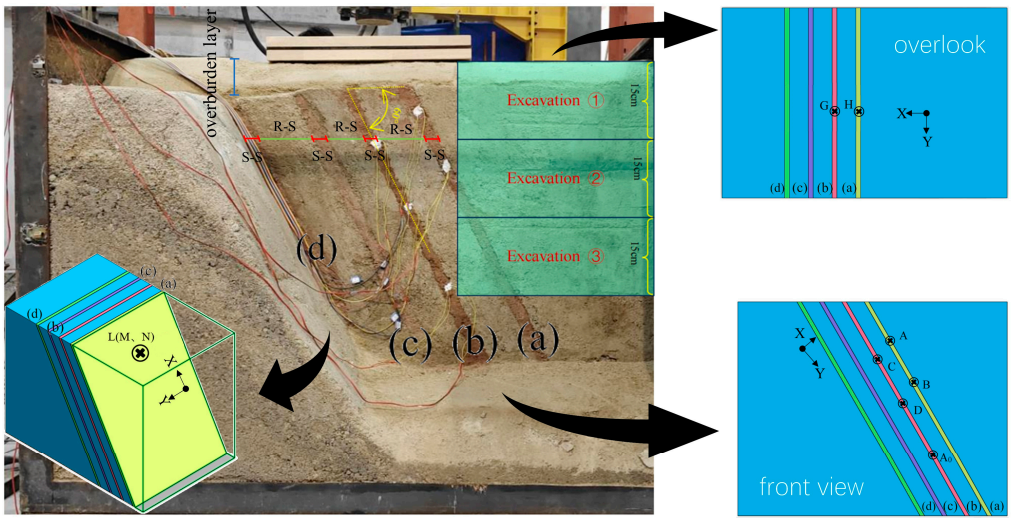

Figure 2. Design scheme of pit physical modeling test.

In Figure 2, the physical test model consists of three main components: the overburden layer, parallel structural surfaces, and rock structure. The overburden is made of medium sand, which is used to transfer the upper loads uniformly to the rock strata. Structural surfaces (a), (b), (c), and (d) are parallel to each other, 2 cm thick, spaced 10 cm apart, and inclined at 60° (this refers to an angle of 60° between the structural plane and the horizontal plane). There is a 10 cm thick rock structure between the two structural surfaces.

The process of constructing the model of the rocky pit in strata with parallel development of structural surfaces was presented below:

(1) A 60° side slope (the material type and material ratio for the slope were the same as those for rock structures) was constructed first. The formwork was then installed according to the thickness of the structural surface. To prevent shifting of the formwork position, wooden sticks and iron pads were used to hold the formwork in place, as shown in Figure 3a.

(2) According to the material ratios of structural surface provided in Table 2, a certain amount of medium sand, cement, gypsum, and water were measured using an electronic scale and then poured into the mixing basin and mixed thoroughly as shown in Figure 3b.

(3) Wooden sticks were used to compact similar material, ensuring that each component had the same density. Once the structural surface was likely strengthened and formed,

the formwork was gradually taken off. A structural surface was conducted as seen in Figure 3c.

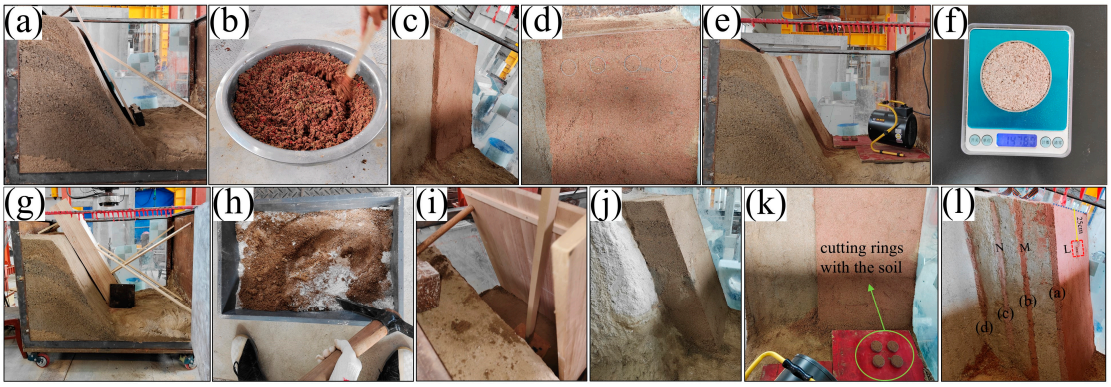

Figure 3. Physical modeling process: (**a**) installed formwork of S-S; (**b**) mixed material of S-S; (**c**) an S-S conducted; (**d**) removed soil; (**e**) drying process; (**f**) measured weight; (**g**) installed formwork of R-S; (**h**) mixed material of R-S; (**i**) compacted material; (**j**) taken off formwork; (**k**) cured structure; (**l**) attached strain gauges.

(4) Soil removed from the structural surface with ring cutters, and any soil removed shall be replaced after removal, as displayed in Figure 3d.

(5) The hot air blower worked and blew hot air. The hot air was used to dry the structural surface and the soil inside the ring cutters, as displayed in Figure 3e.

(6) The weight of the soil inside the ring cutters was measured at 2 h intervals. The drying process can be stopped when the drying weight is reached, as shown in Figure 3f.

(7) The formwork of R-S was then installed according to the thickness of the rock structure. To prevent shifting of the formwork position, wooden sticks and iron pads were used to hold the formwork in place, as seen in Figure 3g.

(8) According to the material ratios of R-S provided in Table 2, a certain amount of medium sand, barite powder, cement, gypsum, and water were measured using an electronic scale and then poured into the mixing box and mixed thoroughly as shown in Figure 3h.

(9) To ensure uniform density and prevent "honeycomb" problems, it must be mixed several times before pouring similar materials into the formwork. As seen in Figure 3i, a rubber hammer was used to compact similar material, ensuring that each component had the same density.

(10) Once the rock structure was likely strengthened and formed, the formwork was gradually taken off. The newly poured structure should not be touched, as depicted in Figure 3j.

(11) Soil was removed from the R-S using cutting rings. The cutting rings with the soil removed were then placed into the pit model box so that it cured in the same condition as the model. The model was heated and dried using a hot air blower as shown in Figure 3k (the drying time was evaluated and regulated by a real-time check of the quality of the cutting rings with the soil).

(12) By repeating steps 1 through 11 above, the modeling of the rock strata can be completed. When the structural surface had reached a certain strength, a groove was dug in the structural surface. A drop of 502 glue was applied to this groove, and a strain gauge was attached, followed by covering the strain gauge with Calvert's waterproofing adhesive and finally backfilling the groove. Point L was located inside the structural surface (a), and its distance along the structural surface (a) to the top surface was 25 cm as shown in Figure 3l. Similarly, points M and N were located

inside structural surfaces (b) and (c), respectively, and their distances along the structural surface to the top surface were all 25 cm. Strain gauges at other points were subsequently pasted. As depicted in Figure 2, points A_0, A, B, C, and D were arranged on the lateral plane of the structural surface. Points G and H were arranged on the surface of the rock layer, and above them was the sandy soil layer. Finally, a layer of medium sand was laid on the rock strata.

2.3. Test Process

The tests included excavation tests of rocky foundations and foundation loading tests.

Figure 4a–c illustrate the excavation procedure of the model excavation test. The pit model was excavated in three steps, each of which was 15 cm deep, with a 10 min interval between excavations. In the first excavation step, the soil layer was excavated, but the structural surface was not excavated. In the second excavation step, the structural surface (a) was completely excavated through. The depth of the pit model after the third excavation was −45 cm, at which point the structural surface (b) had just been excavated through. Photos were captured during the excavation to document and analyze the deformation and settling of the foundation pit. Additionally, strain gauges were utilized to collect strain data from various positions throughout the excavation operation.

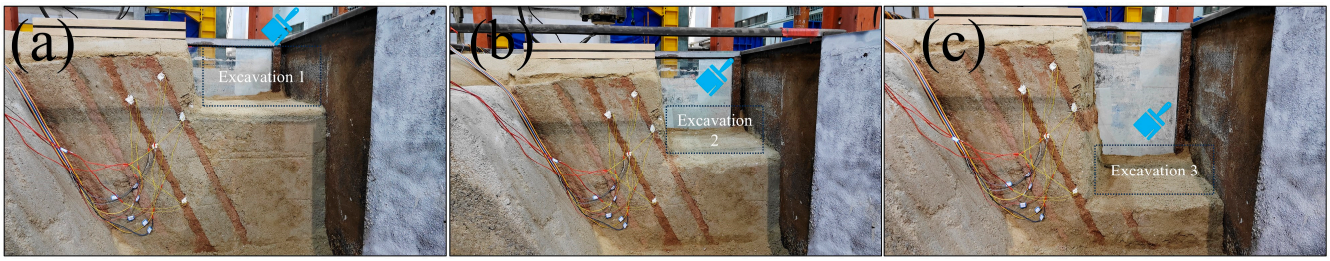

Figure 4. Foundation excavation: (**a**) excavation 1: −15 cm; (**b**) excavation 2: −30 cm; (**c**) excavation 3: −45 cm.

Figure 5 depicts a simplified analytical model of the self-stabilizing height of the upright rock wall of the foundation pit with parallel development of structural surfaces [28]. This analytical model was simplified using approximate planar analysis. The application of Equation (5) is to calculate the theoretical value of the self-stabilizing height (H_{cr}) of the vertical rock wall of the foundation.

$$H_{cr} = \frac{2c}{\gamma \cos\alpha(K\sin\alpha - \cos\alpha\tan\varphi)} - \frac{2q}{\gamma L} \tag{5}$$

where c is the cohesion of the S-S, kN/m^2; K is the safety coefficient; φ is the internal friction angle of the S-S, °; α is the angle of the structural surface and the horizontal plane of the stratum, °; L is the length of the compressed edge, m; and q is the equivalent distributed load, kN/m.

Equation (6) can be converted from Equation (5).

$$q = \frac{cL}{\cos\alpha(K\sin\alpha - \cos\alpha\tan\varphi)} - \frac{\gamma L H_{cr}}{2} \tag{6}$$

In order to better observe and analyze the damage pattern of the pit model, the foundation model was loaded after excavation using an electro–hydraulic servo pressurization system. Based on Equations (5) and (6), and taking into account the mass of the sand layer and the timber matting, calculations showed that the vertical rock wall of the foundation pit can reach a critical self-stabilizing state by providing a force of 3.1 kN. The whole loading

procedure was to first pre-pressurize the test model (its purpose was to compact the soil layer so that it can better transfer the force exerted by the upper electro–hydraulic servo jacks to the lower rock body uniformly), and then the system loaded the force to 3.1 kN and then loaded it to 5 kN, 7 kN, and 9 kN sequentially in 2 min intervals until the physical model was completely destroyed.

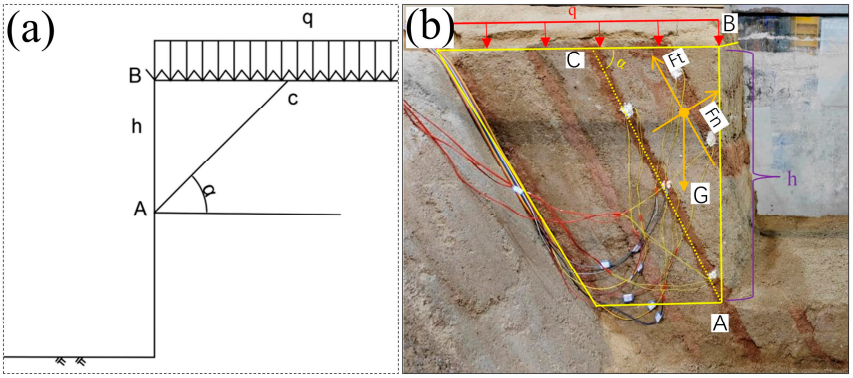

Figure 5. Simplified analytical model: (**a**) analytical model; (**b**) schematic of the model.

2.4. Physical Test Results

2.4.1. Pit Physical Model Excavation Test

As reflected in Figure 4a–c, the settlement deformation of the pit was not readily apparent during the excavation process. Nevertheless, a fissure was discovered on the ground's surface surrounding the pit in Figure 4a. This is due to the concentrated tensile stress at the junction of the sandy soil layer and the rock, and the tensile cracks extend from the structural surface to the sandy soil layer. However, the slip resistance of the structural surface was bigger than the sliding force, which could prevent the occurrence of pit instability, and the stability of the pit was guaranteed.

Figure 6 depicts the strain changes at nine points during excavations. In this figure, "X" refers to the direction perpendicular to the S-S and "Y" refers to the direction parallel to the S-S. In the test, the excavation was carried out in steps of 15 cm, and the duration of each excavation was 10 min. In Figure 6a, the strains at points A, B, C, and D rise and fall once in the first excavation, twice in the second excavation, and once in the third excavation. In the three excavations, the modes of strain are approximately −50, −125, and −250 (mode refers to the number that appears the most frequently). In Figure 6b, the strains at points G and H rise and fall once in the first excavation, twice in the second excavation, and once in the third excavation. In the three excavations, the modes of strain are approximately −50, −125, and −225. In Figure 6c, the strains at points L, M, and N rise and fall once in the first excavation, twice in the second excavation, and once in the third excavation. In the three excavations, the modes of strain are approximately −50, −125, and −250. It can be seen that the strain change rule of these 9 points is basically the same, and the final value of strain is basically around −250. In addition, a strain mutation occurred both at the pit surface and within the structural surface during a single excavation (here the "mutation" is the "rise and fall" described above). However, during the second excavation, the number of strain mutations in strain was more than once as the structural surface was excavated. This can indicate that the presence of structural surface makes it easier for strain mutation to occur during the excavation of foundation pits. In the test of cf. [27], the deformation of the foundation was measured by a handheld 3D scanner. The recorded deformation was not continuous, and it could not record sudden displacement mutations or sudden strain changes during the excavation. The results in Figure 6 are similar to those of Yan Li et al. [29]. Because the structural surface was excavated, rock formations had

deformation mutations inside, and all of them eventually stabilized. Although Yan Li's study was on tunnel excavation works, the stratum in which the tunnels were located was also a parabasic rock strata with parallel structural surfaces.

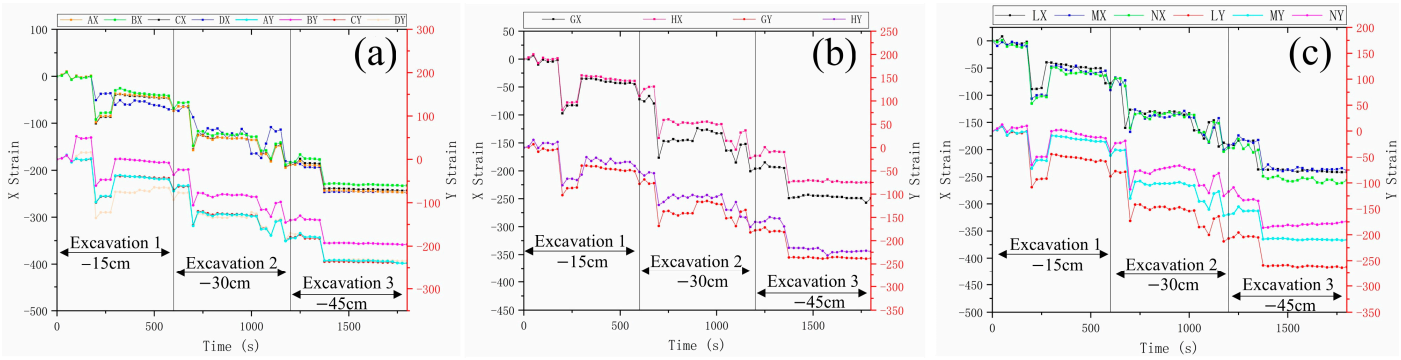

Figure 6. Data on strain gauges in excavation tests: (**a**) data for the points A, B, C, and D; (**b**) data for the points G and H; (**c**) data for the points L, M, and N.

The points on the structural surface had strain mutation, but the plastic zone of the structural surface was not penetrated, which allowed the rocky foundation to remain safe from damage under the self-stabilizing capacity. That was, when the excavation depth of a rocky pit was less than H_{er}, the pit would not destabilize. During the excavation of rocky foundation pits, strains range from −50 to −250, and deformation of the structural surface accumulated.

2.4.2. Pit Physical Model Load Test

Figure 7a–d record the damage process of the foundation under loading, and Figure 7e is a graph of the time-force-displacement relationship made from the electro–hydraulic servo system data. As seen in Figure 7: (1) When the test model was loaded to 3.1 kN, the displacement value was 3.81 mm. At the same time, the cracks in the soil layer were developing, and the cracks were concentrated toward the joint between the S-S (a) and the R-S. (2) When the upper load was increased to 5 kN, the displacement was 4.43 mm. The joint between the structural surface (a) and the rock structure developed into a sliding surface, and the sliding block collapsed along this joint. (3) When the load reached 7 kN, the displacement was 5.89 mm. The number of cracks in the soil layer increased, and all the cracks were also concentrated towards the joint between the S-S (b) and the R-S (this joint became a potential sliding surface). (4) When the load reached 9 kN not long after, the potential sliding surface, the joint between the S-S (b) and the R-S, collapsed along the S-S.

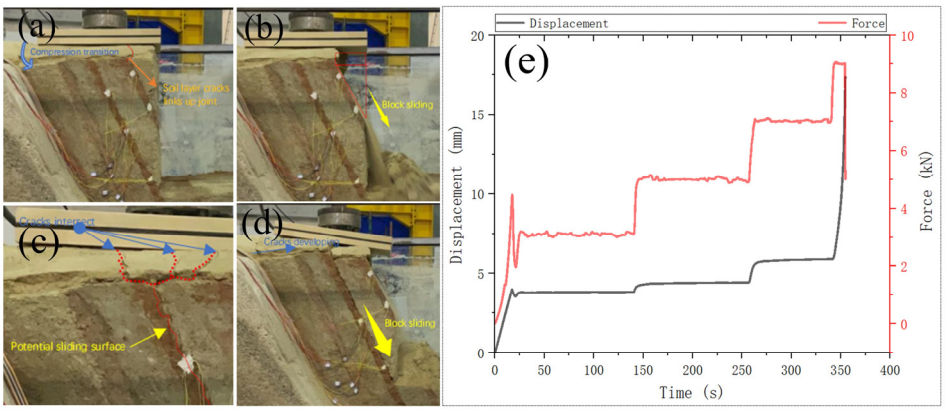

Figure 7. Foundation loading test: (**a**) load 3.1 kN; (**b**) load 5 kN; (**c**) load 7 kN; (**d**) load 9 kN; (**e**) load and displacement data from electrohydraulic servo system.

In the excavation test of the rocky foundation with parallel development of structural surfaces, the excavation depth was less than the critical safe height H_{er} of the rocky foundation, and the foundation was not destabilized under the self-stabilizing capacity. Cracks in the sandy soil layer extended toward the potential sliding surface. And the deformation within the S-S was accumulating. In the loading test of the rocky foundation with parallel development of structural surfaces, the load was increased from 0 to 3.1 kN, and the displacement of the pit surface increased abruptly. In this process, the deformation of the S-S (a) proceeded with considerable accumulation, and the internal plastic zone developed rapidly. Although the pit model had reached a critical state, the potential sliding surface (the joint between the S-S (a) and R-S) had not yet been fully penetrated, and the points on the potential sliding surface had not been subjected to displacement mutation. When the load was increased by 5 kN, the points on this sliding surface quickly underwent displacement mutation. The rock structure above the S-S) became a sliding block and suddenly collapsed, and destabilization damage occurred in the rocky foundation. In three dimensions, this destabilizing damage would be constrained by the surrounding geotechnical body and form a wedge-shaped damage. When the load changed from 5 kN to 7 kN, the number of cracks in the sandy soil layer increased, and all of them extended towards the potential sliding surface (the joint between the S-S (b) and R-S). At the same time, a large displacement of the pit surface occurred at this stage (displacement increment of 1.46 mm), and a considerable accumulation of deformation of the structural surface (b) was carried out. When the load reaches 9 kN, the plastic zone of the potential sliding surface was penetrated, and displacement mutation occurred, and then the sliding block collapsed along the S-S (b). Therefore, we divided the damage process of rocky foundations with parallel development of structural surfaces into three stages: soil crack development stage, structural surface deformation accumulation stage, and sliding block collapse.

3. Numerical Simulation and Analysis

3.1. Numerical Simulation Model

Numerical calculation was performed using the Midas GTS NX 2022 R1(x64) software. The Midas GTS program was used to compute the pit numerically. Numerical modeling was performed as a two-dimensional model. The width of the pit was 30 m, and the depth was 22.5 m (45 cm × 50 = 22.5 m). The structural planes in the strata developed parallel, with a dip angle of 60° and a thickness of 1 m (2 cm × 50 = 1 m). The thickness of the rock mass structure was 5 m (10 cm × 50 = 5 m). The boundary dimensions of the model were 320 m × 140 m, as shown in Figure 8. The model materials were all modeled using the Mohr–Coulomb model with the property of 2D plane strain type. The specific parameters of the model material were given in Table 1 for raw material. Grid sizes of 0.5 m and 1.2 m were used for excavated S-S and R-S, and 0.9 m and 1.6 m for unexcavated S-S and R-S. In this way, the whole model was divided into 42,495 2D grid cells. The boundary constraints of the model were automatic boundary constraints, and the model was assigned a self-weight load (gravity) and line loads. Other factors, such as groundwater and seismic effects, were not taken into account.

The numerical simulation was divided into two distinct working conditions: the calculation model for pit excavation and the calculation model for loads after the pit was excavated.

The model was constructed using the following six steps in sequence: Step 1 was to create a 2D wireframe representation of the model, starting from the origin (0,0) in the spatial interface of the Midas GTS software. After the pit model wireframe was drawn, the cross-segmentation command was used to segment all the cross-lines so that later meshing could proceed smoothly; Step 2 was to define the model material and model property; Step 3 was to divide the mesh.

The depth of the pit model was 22.5 m, and the excavation was carried out three times, as shown in the lower right corner in Figure 8. The three rock layers that were excavated were first meshed sequentially, and then the unexcavated rock layers were meshed. All 2D grid cells must be meshed in order to avoid that the model does not operate properly; Step 4 was to assign automatic boundary constraints, gravity, and line loads. In the physical modeling tests, the applied loads were 3.1 kN, 5 kN, 7 kN, and 9 kN. These loads were converted into line loads and multiplied by C_q to obtain 43.92 kN/m, 70.83 kN/m, 99.17 kN/m, and 127.5 kN/m, i.e., those were the line loads imposed by the numerical simulation; Step 5 was to define the construction phases. The construction phases were defined as eight phases, which were initial stress field equilibrium (this included activating the gravity and automatic boundary constraints and setting the displacement to 0), Excavation 1 (pit depth −7.5 m), Excavation 2 (pit depth 15 m), Excavation 3 (pit depth 22.5 m), applying line load 1 (43.92 kN/m), applying line load 2 (70.83 kN/m), applying line load 3 (99.17 kN/m), and applying line load 4 (127.5 kN/m); and Step 6 was to create the construction phase analysis and perform the computational analysis.

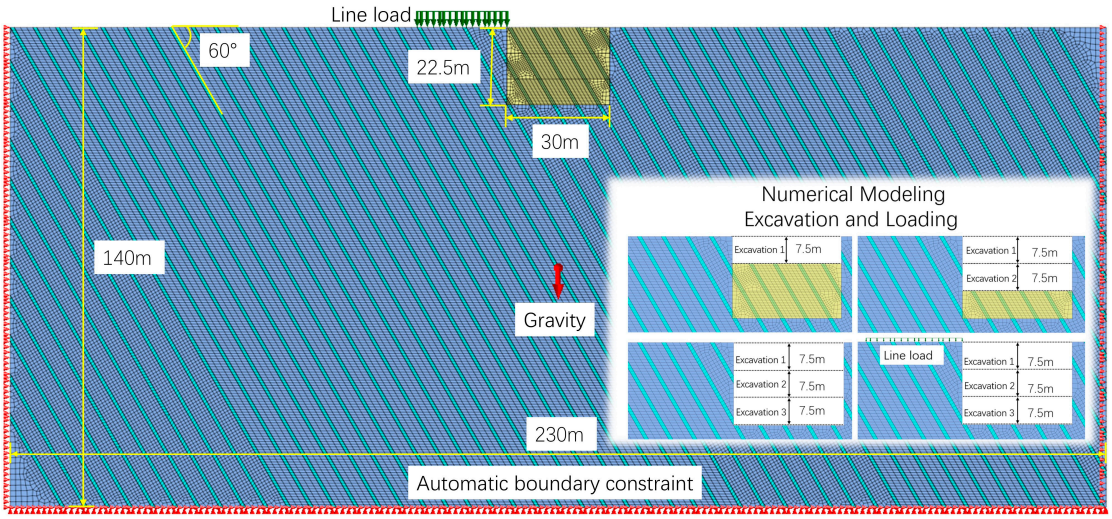

Figure 8. Numerical simulation model.

3.2. Result of Computational Analysis

The variation of maximum displacement values of rocky foundation pits during excavation is depicted in Figure 9a. From excavation 0 m to excavation −22.5 m, the maximum displacement value of the rocky pit increased from 0 to 58.57 mm. The depth of all three excavations was 7.5 m. The increment of the maximum displacement value of the first two excavations was about 18 mm, but the maximum displacement value of the latter excavation was 5.56 mm bigger than 18 mm. This was due to the fact that one of the structural surfaces was fully excavated, and its presence would have caused larger displacements in the pit excavation. This is similar to the results of the excavation tests in the physical model tests: as the structural surface (a) is excavated, the number of mutations in the strain of the rocky foundation is increased. The variation of maximum displacement values of the rocky foundation pit during loading is demonstrated in Figure 9b. The linear load increased from 43.92 kN/m to 127.5 kN/m, and the maximum displacement value of the pit increased from 58.57 mm to 92.26 mm. The increments of the maximum displacement values of the pit in the four loadings were 1.67 mm, 3.99 mm, 12.37 mm, and 15.65 mm, respectively. After both the second and fourth loadings, the change in the maximum displacement value of the pit was much larger than the previous one. This is because the pit has sliding blocks collapsing at these two times.

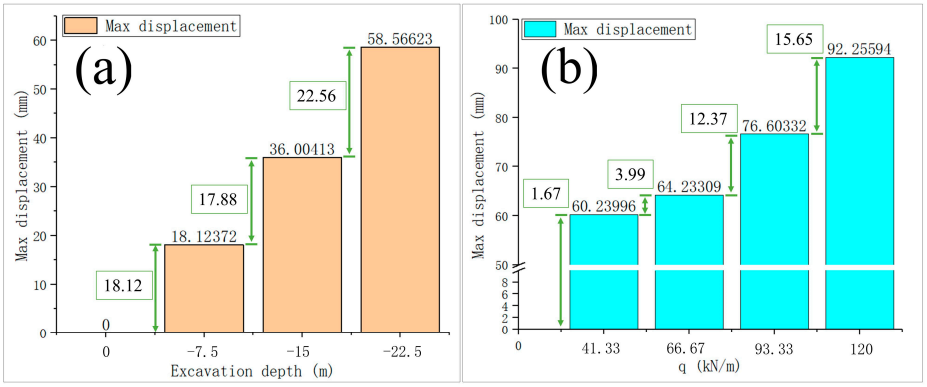

Figure 9. Maximum displacement values for rocky foundation excavation and loading: (**a**) maximum displacement of excavation; (**b**) maximum displacement of loading.

Figure 10 depicts the change in the plastic zone of the foundation pit during loading. The plastic zone of the S-S of the pit was not penetrated when the applied load was 43.92 kN/m; the plastic zone of the first excavated S-S was penetrated when the applied load was 70.83 kN/m. The maximum displacement value of the rocky foundation was larger than the previous one, and the point where the maximum displacement occurred was on the first excavated S-S. This means that the point on the potential sliding surface undergoes displacement mutation, the pit undergoes destabilizing damage, and the rock structure on the sliding surface collapses along the first excavated S-S; When the applied load was increased to 99.17 kN/m, the plastic zone of the second excavated structural surface gradually developed, but the plastic zone was not completely penetrated; When the applied load was increased to 127.5 kN/m, the plastic zone of the second excavated S-S was completely penetrated, displacement mutation occurred at points on the potential sliding surface, and the rock structure on the sliding surface collapsed along the second excavated S-S.

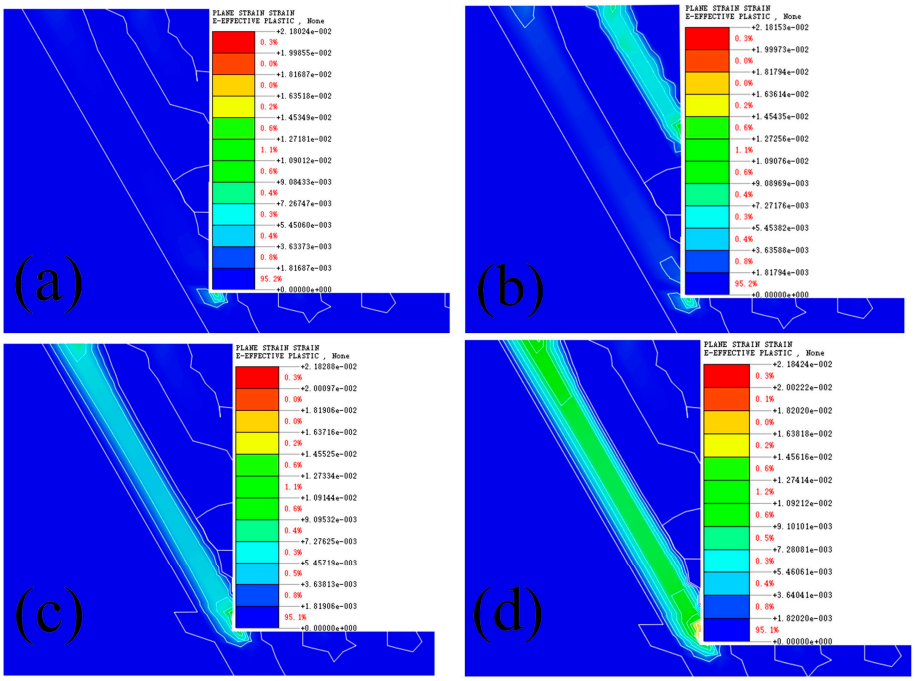

Figure 10. Foundation plasticity zone development diagram: (**a**) load 43.92 kN/m; (**b**) load 70.83 kN/m; (**c**) load 99.17 kN/m; (**d**) load 127.5 kN/m.

4. Discussion

Physical tests and numerical simulations of the damage mechanism of rocky foundations with parallel structural surfaces had some practical significance. The study is conducive to comprehending and understanding the excavation deformation law and destabilization damage mechanism of foundations with parallel structural surfaces. It can provide construction ideas, support structure design options, risk prediction, etc., for similar foundation projects. The deformation evolution law and destabilization damage mechanism of geotechnical structures were the core points of analyzing foundation slope engineering. Chen Ding et al. [30] researched the deformation mechanism of the stratified rock and soil slope based on long-term monitoring data. And established a geological model of a high and very steep slope using FLAC^{3D} to evaluate its stability. The internal spatial evolution effect of the deformation was well demonstrated. However, the destabilizing and destructive process of this rock structure had not been well examined. In the physical tests, the damage evolution law when the geotechnical structure model was completely destroyed would be well studied. In this paper, physical model excavation and loading tests were carried out on a foundation with parallel structural surfaces, and the model of the geotechnical structure was completely destabilized and damaged during the tests. The destabilizing damage of rocky foundations in strata with parallel-developed structural surfaces can be divided into three stages: soil crack development stage, structural surface deformation accumulation stage, and sliding block collapse. When the pit excavation was completed, cracks developed within the soil layer and propagated in the direction of the potential sliding surface (the joint between the first excavated S-S and the R-S). When the foundation pit was loaded to critical safety, the plastic zone of the first excavated structural surface was not penetrated (as shown in Figure 10a), and the deformation of this S-S was accumulating. This plastic zone was penetrated when the load was applied further (as shown in Figure 10b). A displacement mutation occurred at the upper point of the potential sliding surface, and the rock structure on the upper part of the first excavated S-S turned into a sliding block, which collapsed along the S-S (as shown in Figure 7b). As the load reloading continues to increase, the deformation of the second excavated structural surface accumulated, and its plastic zone developed (as shown in Figure 10c). When the load was increased further, the plastic zone was completely penetrated (as shown in Figure 10d). A displacement mutation occurred at the point on the potential sliding surface (the joint between the second excavated S-S and the R-S), and the sliding block collapsed along the S-S.

In fact, the distribution of laminated rock formations is widespread, and the stratigraphic situation is quite complex. This makes the practical engineering work very challenging. Laminated rock formations can be classified according to the dip β of the structural surface: horizontal formations ($0° < \beta < 5°$), gently dipping formations ($5° < \beta < 20°$), sharply dipping formations ($20° < \beta < 45°$), steeply dipping formations ($45° < \beta < 85°$), upright formations ($85° < \beta < 90°$), and anticlinal formations (β greater than 90°). The thickness of the structural surface, strength parameters, spacing, degree of development, etc. can have a great impact on the stability analysis and support design of foundation slope works. In the actual rocky foundation project, this type of foundation pit is recommended to use the support form of steel pipe pile with a soil nail wall. If the upper part of the rock strata has different thicknesses of soil layer, the combined support form of steel pipe pile + bored pile + high-pressure rotary spray pile can be adopted. In addition, the groundwater changes, earthquakes, weathering, and other effects on the foundation slope engineering cannot be ignored. The study will incorporate dynamic properties such as earthquakes and blasting, groundwater, and rainfall. The study will be further enriched, closer to reality, and better guided for engineering practice.

5. Conclusions

In this thesis, physical model tests and numerical simulations of rocky foundations in strata with parallelly developed structural surfaces are carried out to obtain the following conclusions:

(1) Due to the influence of the self-stabilizing capacity of the foundation, the excavation of rocky foundation in strata with parallel developed structural surfaces can basically satisfy the stability requirements if the depth of foundation excavation is less than the critical height of foundation self-stabilization. In the physical model excavation tests, the strain values of the strain gauges increased in stages within 0–250. It makes rocky foundation more susceptible to strain mutations or displacement mutations during excavation because of the presence of structural surfaces.

(2) In physical experiments and numerical simulations of foundation loading, the increment of the maximum displacement value at the surface of the foundation accelerates with a uniform increase in the load value (1.67 mm→3.99 mm→12.37 mm→15.65 mm). When the loads reached 70.83 kN/m (5 kN) and 127.5 kN/m (7 kN), the plastic zone of the first and second structural surfaces was completely penetrated, and the sliding body collapsed, respectively.

(3) The damage mechanisms of rocky foundations in strata with parallelly developed structural surfaces: The soil in the upper part of the rock strata will crack first, and the cracks will extend toward the potential sliding surface (the joint between the excavated structural surface and the rock structure). The deformation within the structural surface then accumulates and the plastic zone of the structural surface develops. When the plastic zone is penetrated, the points on the potential sliding surface undergo displacement mutations, and the sliding block collapses along the structural surface. The instability and failure of this type of foundation pit can be divided into three stages: soil crack development stage, structural surface deformation accumulation stage, and sliding block collapse.

Author Contributions: Conceptualization, Z.Z. and W.L.; Data curation, W.L.; Methodology, Z.Z.; Formal analysis, W.L. and A.H.; Investigation. A.H. and L.W.; Writing—original draft, W.L.; Writing—review and editing, Z.Z.; Supervision, Z.Z.; Project administration, Z.Z.; Resources, Z.Z.; Software, W.L., A.H. and L.W.; Supervision, Z.Z.; Validation, W.L., A.H. and L.W.; Visualization, A.H. and W.L. All authors have read and agreed to the published version of the manuscript.

Funding: This study was funded by the Provincial Natural Science Research Project of colleges and universities in Anhui Province-Key projects (KJ2021A0611), the Science and Technology Plan of Housing and Urban-Rural Construction in Anhui Province (2022-YF096, 2020-YF038), and Science and technology development project (HYB20240110, HYB20190152, HYB20220092, HYB20220162).

Data Availability Statement: The data used to support the findings of this study are available from the corresponding author upon request.

Conflicts of Interest: The authors declare that they have no conflicts of interest.

References

1. Sabermahany, H.; Attarnejad, R. Seismic performance of buildings supported by a shallow doubly-curved shell raft foundation. *Structures* **2022**, *36*, 619–634. [CrossRef]
2. Ter-Martirosyan, Z.G.; Ter-Martirosyan, A.Z.; Vanina, Y.V. Mathematical Analysis for the Evaluation of Settlement and Load-Bearing Capacity of a Soil Base Adjacent to an Excavation Pit. *Axioms* **2022**, *11*, 353. [CrossRef]
3. Ramm, H.; Reul, O.; Ruiken, A.; Kissel, W.; Toker, E. Hochhaus Omniturm-Baugrube und Grundung unter komplexen innerstadtischen Randbedingungen. *Bautechnik* **2020**, *97*, 656–663. [CrossRef]
4. Yan, W.; Yang, C.; Zuo, J.M.; Cheng, J.Q. Stability calculation of soil excavation in soil and rock foundation pits. *J. Undergr. Space Eng.* **2015**, *11*, 246–250.

5. Asadizadeh, M.; Moosavi, M.; Hossaini, M.F.; Hedayat, A.; Sherizadeh, T.; Masoumi, H. Numerical Modeling of Rock Blocks with Nonpersistent Rough Joints Subjected to Uniaxial Compressive and Shear Loadings. *Int. J. Geomech.* **2023**, *23*, 04023103. [CrossRef]
6. Vaziri, M.R.; Tavakoli, H.; Bahaaddini, M. 2D numerical study of the mechanical behaviour of non-persistent jointed rock masses under uniaxial and biaxial compression tests. *Geomech. Eng.* **2022**, *28*, 117–133.
7. Zhang, J.T.; Kikumoto, M.; Yasuhara, H.; Ogata, S.; Kishida, K. Modeling the shearing behavior of discontinuous rock mass incorporating dilation of joint aperture. *Int. J. Rock Mech. Min. Sci.* **2022**, *153*, 105101. [CrossRef]
8. Al-E'Bayat, M.; Guner, D.; Sherizadeh, T.; Asadizadeh, M. Numerical Investigation for the Effect of Joint Persistence on Rock Slope Stability Using a Lattice Spring-Based Synthetic Rock Mass Model. *Sustainability* **2024**, *16*, 894. [CrossRef]
9. Zhang, H.J.; Wu, S.C.; Zhang, Z.X.; Huang, S.G. Reliability analysis of rock slopes considering the uncertainty of joint spatial distributions. *Comput. Geotech.* **2023**, *161*, 105566. [CrossRef]
10. Hua, D.J.; Jiang, Q.H. A general equivalent continuum model and elastic wave velocity analysis of jointed rock masses. *Int. J. Rock Mech. Min. Sci.* **2023**, *170*, 105500. [CrossRef]
11. Wang, J.T.; Zuo, J.P. Numerical simulation on effect of heterogeneity on mode I fracture characteristics of rock. *J. Cent. South Univ.* **2020**, *27*, 3063–3077. [CrossRef]
12. Zhu, L.F.; Wang, L.Q.; Zheng, L.B.; Xie, N.; Wang, C.S.; Sun, Z.H.; Wang, C.L.; Wu, S.B.; Fan, B.Q. Shear creep characteristics and creep constitutive model of bolted rock joints. *Eng. Geol.* **2023**, *327*, 107368. [CrossRef]
13. Xu, J.; Wang, Y.S.; Li, C.C. Stability analysis of rock slope and calculation of rock lateral pressure in foundation pit with structural plane and cave development. *Sci. Rep.* **2022**, *12*, 8710. [CrossRef] [PubMed]
14. Xu, J.; Wang, Y.S. Stability Analysis and Support Design Methods for Rock Foundation Pit with Combination of Structural Plane and Karst Cave. *Adv. Civ. Eng.* **2022**, *2022*, 5662079. [CrossRef]
15. Wang, C.W.; Liu, X.L.; Song, D.Q.; Wang, E.Z.; Zhang, J.M. Elasto-plastic analysis of the surrounding rock mass in circular tunnel using a new numerical model based on generalized nonlinear unified strength theory. *Comput. Geotech.* **2023**, *154*, 105163. [CrossRef]
16. Yeh, P.T.; Chen, I.H.; Lee, K.Z.Z.; Chang, K.T. Graphical comparison of numerical analysis, slope mass rating, and kinematic analysis for the effects of weak plane orientations on rock slope stability. *Eng. Geol.* **2022**, *311*, 106900. [CrossRef]
17. Guo, H.; Yan, C.Z.; Zhang, G.H.; Xu, R.; Wang, T.; Jiao, Y.Y. Mechanical analysis of toppling failure using FDEM: A case study for soft-hard interbedded anti-dip rock slope. *Comput. Geotech.* **2024**, *165*, 105883. [CrossRef]
18. Pajalic, S.; Peranic, J.; Maksimovic, S.; Ceh, N.; Jagodnik, V.; Arbanas, Z. Monitoring and Data Analysis in Small-Scale Landslide Physical Model. *Appl. Sci.* **2021**, *11*, 5040. [CrossRef]
19. Lozada, C.; Mendoza, C.; Amortegui, J.V. Physical and Numerical Modeling of Clayey Slopes Reinforced with Roots. *Int. J. Civ. Eng.* **2022**, *20*, 1115–1128. [CrossRef]
20. Benemaran, R.S.; Esmaeili-Falak, M.; Katebi, H. Physical and numerical modelling of pile-stabilised saturated layered slopes. *Proc. Inst. Civ. Eng. Geotech. Eng.* **2022**, *175*, 523–538.
21. Ghamkhar, G.; Johari, M.S.; Bodaghi, M. Enhancing damage resistance in tubular triaxial hybrid braided composites: Innovative production and tensile modulus prediction with damage analysis. *Polym. Compos.* **2024**, *45*, 8119–8132. [CrossRef]
22. Hu, X.Y.; Fang, Y.; Walton, G.; He, C. Analysis of the behaviour of a novel support system in an anisotropically jointed rock mass. *Tunn. Undergr. Space Technol.* **2019**, *83*, 113–134. [CrossRef]
23. Moussaei, N.; Sharifzadeh, M.; Safiriar, K.; Khosravi, M.H. A new classification of failure mechanisms at tunnels in stratified rock masses through physical and numerical modeling. *Tunn. Undergr. Space Technol.* **2019**, *91*, 103017. [CrossRef]
24. Qiu, J.; Zhou, X.; Shen, Y.; Zhang, X.; Yu, B.; Luo, Y.S. Failure mechanism of the deep-buried metro tunnel in mixed strata: Physical model test and numerical investigation. *Tunn. Undergr. Space Technol.* **2023**, *139*, 105224. [CrossRef]
25. Wang, J.; Liu, P.; Wu, C.; He, M.; Gong, W. Mechanical behavior of soft rock roadway reinforced with NPR cables: A physical model test and case study. *Tunn. Undergr. Space Technol.* **2023**, *138*, 105203. [CrossRef]
26. Wei, G.; Qi, Y.; Chen, C.; Zhang, S.; Qian, C.; Zhou, J. Analysis of the protective effect of setting isolation piles outside the foundation pit on the underpass tunnel side. *Transp. Geotech.* **2022**, *35*, 100791. [CrossRef]
27. Zhang, Z.; You, X.; Zhang, C.; Li, W.; Zhang, M. Study on the critical stable height of vertical excavation in rocky foundation pit within layered structural plane. *Sci. Rep.* **2024**, *14*, 12191. [CrossRef]
28. Ziguang, Z.; Li, Y.; Zhang, J.; Xu, T.; Cao, G.; Xu, Y. Study on the Characteristics of Self-Stabilizing Height Distribution for Deep Foundation Pit Vertical Sidewall in Binary Strata of Upper Soil and Lower Rock. *Adv. Civ. Eng.* **2021**, *2021*, 5411703. [CrossRef]

29. Li, Y.; Qi, T.; Lei, B.; Qian, W.; Li, Z. Deformation Patterns and Surface Settlement Trough in Stratified Jointed Rock in Tunnel Excavation. *KSCE J. Civ. Eng.* **2019**, *23*, 3188–3199. [CrossRef]
30. Ding, C.; Xue, K.X.; Zhou, C.H. Deformation analysis and mechanism research for stratified rock and soil slope. *Bull. Eng. Geol. Environ.* **2024**, *83*, 300. [CrossRef]